ELSEVIER

Journal of Fluids and Structures 26 (2010) 780–792

JOURNAL OF
FLUIDS AND
STRUCTURES

www.elsevier.com/locate/jfs

A shallow-depth sloshing absorber for structural control

A.P. Marsh[a,*], M. Prakash[b], S.E. Semercigil[a], Ö.F. Turan[a]

[a] *Victoria University, School of Architectural, Civil and Mechanical Engineering, Melbourne, VIC 3011, Australia*
[b] *CSIRO Mathematical and Information Sciences, Private Bag 33, Clayton, VIC 3168, Australia*

Received 22 June 2009; accepted 14 March 2010
Available online 13 May 2010

Abstract

Sloshing absorbers work on a similar principle to that of tuned vibration absorbers. A sloshing absorber consists of a tank, partially filled with liquid. The absorber is attached to the structure to be controlled, and relies on the structure's motion to excite the liquid. Consequently, a sloshing wave is produced at the liquid free surface possessing energy dissipative qualities. The primary objective of this paper is to demonstrate the effectiveness of employing liquid sloshing as a structural control mechanism. To this end, simple experimental observations are presented first. Then, numerical predictions obtained using smoothed particle hydrodynamics (SPH) are compared with experimental observations. The objective of this comparison is to demonstrate the modelling technique's ability to approximate the characteristics of such flows.

Keywords: Liquid sloshing; Structural control; Smoothed particle hydrodynamics; Hydraulic jump

---

1. Introduction

Sloshing is the low frequency oscillation of a liquid within a partially full container. The controlling of sloshing has generally been directed towards suppression due to the damaging effects it can impose (Popov et al., 1993; Faltinsen, 1993). Shekari et al. (2008) used a coupled boundary element–finite element formulation to analyse the dynamic behaviour of a cylindrical storage tank on a rigid foundation during seismically induced vibrations. More recently, Curadelli et al. (2010) used measurements and finite element simulations to evaluate the influence of liquid levels on the structural response in elevated spherical containers typically used as liquefied petroleum gas (LPG) storage tanks. It is also possible to employ sloshing as an effective energy sink in various engineering applications to provide protection for structures exposed to excessive vibration levels (Sun and Fujino, 1994; Modi et al., 1996; Tamura et al., 1996; Modi and Munshi, 1998; Tait et al., 2005). A recent review by Païdoussis (2008) provides an excellent resource for understanding such fluid–structure interaction problems: the book by Axisa and Antunes (2007).

A tuned liquid damper (TLD) can act as a damped dynamic vibration absorber as shown in Fig. 1. A TLD is simply a container attached on the structure to be controlled. Sloshing in the container is induced intentionally for structural control. Generally, the absorber is tuned so that the frequency of sloshing normally coincides with the natural frequency of the structure (Kareem, 1990; Banerji et al., 2000). When designed properly, the sloshing fluid oscillates out of phase from mass

---

[*] Corresponding author. LMF Ecole Centrale de Nantes, 1 rue de le Nöe 44300 Nantes, France.
E-mail addresses: Adam.Marsh@ec-nantes.fr, adampmarsh@gmail.com (A.P. Marsh).

0889-9746/$ - see front matter © 2010 Elsevier Ltd. All rights reserved.
doi:10.1016/j.jfluidstructs.2010.03.006

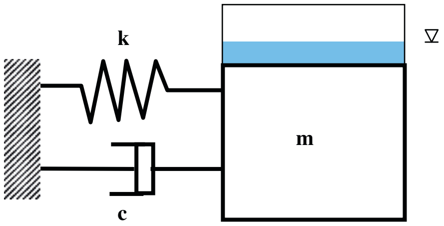

Fig. 1. Sloshing absorber, attached to a mechanical oscillator of mass m, stiffness k, and viscous damping coefficient of c.

m, creating a counteracting pressure force on the side of the container. Shearing of the fluid is the primary form of mechanical damping in this type of absorber, providing that the liquid level is low (Kareem, 1990; Marsh, 2009).

Investigating an effective means of using intentionally induced liquid sloshing for structural control applications is the primary objective of this paper. Simple experiments are described next involving a sloshing absorber. The objective of the experiments is to establish the sloshing absorber as a promising controller of light and resonant structures. In addition, experimental observations are useful to determine the effect of varying liquid depth on structural control.

There are two objectives of the numerical work. The first is to test the accuracy of the predicted free surface, through comparisons with experimental observations. The second objective is to demonstrate the potential ability of SPH to model fluid–structure interactions. The validated numerical model can then be used for design and optimisation of such structural control devices. The reported cases where the experimentally observed container motion is imposed should be interpreted as the first stage of a full fluid–structure interaction, where the motion of the container is the result of the structural response to sloshing fluid forces. Full interaction is the subject of the next phase of investigation.

2. Numerical model

Smoothed particle hydrodynamics (SPH) is used in this study to model two-dimensional liquid sloshing absorbers. SPH is a Lagrangian method of solving the equations of fluid flow, suitable for modelling liquid sloshing due to its grid-free nature, and inherent ability to model complex free surface behaviour. SPH has been successfully applied to a wide range of industrial fluid flow applications (Cleary et al., 2006, 2007). A detailed description of the method can be found in Monaghan (1992).

In SPH, the fluid being modelled is discretized into fluid elements or particles, the properties of which are attributed to their centres. The method works by tracking particles and approximating them as moving interpolation points. These fluid particles (or moving interpolation points) have a spatial distance over which field variables such as density, velocity, and energy are smoothed. This is achieved via an interpolation kernel function.

The fundamental concept of the integral representation of a function used in the SPH method comes from the identity

$$f(x) = \int_V f(x')\delta(x-x')\,dx'. \tag{1}$$

The identity implies that a function can be represented in integral form. Here $f(x)$ is a function of the three-dimensional position vector x, V is the volume of the integral that contains x, and $\delta(x-x')$ is the Dirac delta function,

$$\delta(x-x') = \begin{cases} 1, & x = x', \\ 0, & x \neq x'. \end{cases} \tag{2}$$

The integral representation in Eq. (1) is exact since the delta function is used, providing that $f(x)$ is defined and continuous in V (Liu and Liu, 2003). In SPH the Dirac delta function is replaced by the smoothing function $W(x-x',h)$ so that the integral representation of $f(x)$ is specified as

$$\langle f(x) \rangle = \int_V f(x')W(x-x',h)\,dx', \tag{3}$$

where W is the interpolation kernel, h is the smoothing length that defines the region in which the smoothing function operates. A cubic smoothing kernel has been used here for $W(x-x',h)$, approximating the shape of a Gaussian profile but having compact support, so that $W(x-x',h) = 0$ for $x-x' > h$.

The integral representation of the spatial derivative of a function in SPH is performed in the same way. $f(x)$ is substituted for $\nabla \cdot f(x)$ in Eq. (3) to produce

$$\langle \nabla \cdot f(x) \rangle = \int_V \nabla \cdot f(x') W(x-x',h)\, dx'. \tag{4}$$

From the identity in

$$[\nabla \cdot f(x')] W(x-x',h) = \nabla \cdot [f(x') W(x-x',h)] - f(x') \nabla \cdot W(x-x',h), \tag{5}$$

one obtains

$$\langle \nabla \cdot f(x) \rangle = \int_V [\nabla \cdot f(x') W(x-x',h)]\, dx' - \int_V f(x') \nabla \cdot W(x-x',h)\, dx'. \tag{6}$$

The first integral on the right-hand side of Eq. (6) is converted using the divergence theorem of Gauss to give

$$\langle \nabla \cdot f(x) \rangle = \int_S f(x') W(x-x',h) \cdot \vec{n}\, \mathbf{dS} - \int_V f(x') \nabla \cdot W(x-x',h)\, dx'. \tag{7}$$

Here, S is the surface of the integration domain V, $\vec{n}$ is the unit normal to the domain surface S. When the support domain of W is located within the problem domain, the first integral on the right-hand side of Eq. (7) is zero. However, when the support domain overlaps with the problem domain, W is truncated by the problem domain boundary, hence, the surface integral is no longer zero. For all points in space whose support domain lies within the problem domain, Eq. (7) simplifies to

$$\langle \nabla \cdot f(x) \rangle = -\int_V f(x') \nabla \cdot W(x-x',h)\, dx'. \tag{8}$$

For all other points in space, modifications need to be made to treat the boundary effects if the surface integral is to be equated to zero (Liu and Liu, 2003). Eq. (8) states that the spatial gradient of a function is determined from the values of the function and the derivative of the smoothing function, rather than the derivative of the function itself.

Discretization is performed by converting the integral representations in Eqs. (3) and (8) into summations over all the particles that lie within the support domain of W. This is achieved by replacing the infinitesimal volume dx' by the finite volume of particle j, ΔV_j. The mass of particle $j(m_j)$ is then related to this volume by

$$m_j = \rho_j \Delta V_j, \tag{9}$$

where ρ_j is the density of particle j. The discretized particle approximation can then be written as

$$\langle f(x_i) \rangle = \sum_{j=1}^{N} \frac{m_j}{\rho_j} f(x_j) W(x_i - x_j, h). \tag{10}$$

Eq. (10) states that the value of a function at particle i is approximated using the average of the same function at all j particles within the support domain of particle i, weighted according to the smoothing function. The same approach is used to produce the particle approximation of the spatial derivative of a function,

$$\langle \nabla \cdot f(x_i) \rangle = -\sum_{j=1}^{N} \frac{m_j}{\rho_j} f(x_j) \cdot \nabla W(x_i - x_j, h), \tag{11}$$

∇W is taken with respect to particle j in Eq. (11), when taken with respect to particle i the negative sign is removed, producing

$$\langle \nabla \cdot f(x_i) \rangle = \sum_{j=1}^{N} \frac{m_j}{\rho_j} f(x_j) \cdot \nabla_i W(x_i - x_j, h). \tag{12}$$

The SPH approximations in Eqs. (10) and (12) are applied to the field variables and their derivatives within the Lagrangian equations of fluid flow. This yields the continuity and momentum equations

$$\frac{d\rho_i}{dt} = \sum_{j=1}^{N} \frac{m_j}{\rho_j} v_{ij} \nabla_i W_{ij}, \tag{13}$$

$$\frac{dv_i}{dt} = -\sum_{j=1}^{N} m_j \left[\left(\frac{P_j}{\rho_j^2} + \frac{P_i}{\rho_i^2} \right) - \frac{\xi}{\rho_i \rho_j} \frac{4\mu_i \mu_j}{(\mu_i + \mu_j)} \frac{v_{ij} r_{ij}}{r_{ij}^2 + \eta^2} \right] \nabla_i W_{ij} + g, \tag{14}$$

where $W_{ij} = W(r_{ij},h)$ and is evaluated for the distance $|r_{ij}|$. r_{ij} is the position vector from particle 'j' to particle 'i' and is equal to $r_i - r_j$.

The first term within the square brackets is pressure. The term on the right, without ξ, is artificial viscosity. This term is used to increase the stability of the numerical algorithm (Colagrossi, 2005); ξ is a proportionality factor that relates the artificial viscosity to the real SPH viscosity, and has a theoretical value of 4, but has been modified empirically to 4.96333 (Cleary, 1998). ξ has values of between 4 and 5 for most applications. P_i and μ_i are the pressure and viscosity of particle 'i'; the same applies for particle 'j'; $v_{ij} = v_i - v_j$; η is a parameter used to smooth out the singularity at $r_{ij} = 0$, and g is the body force acceleration due to gravity.

The code uses a compressible method for determining the fluid pressure. It is operated near the incompressible limit by selecting a speed of sound that is much larger (around 10 times) that of the velocity scale expected in the fluid flow. Eq. (15) governs the relationship between particle density and fluid pressure,

$$P = P_0 \left[\left(\frac{\rho}{\rho_0} \right) - 1 \right]. \tag{15}$$

This equation is a modified version of that used in Batchelor (1967) to accurately describe sound wave propagation. A much lower speed of sound is used here to reduce computational expense as given in Eq. (16) below, without physical penalty. Here P is the magnitude of the pressure and ρ_0 is the reference density, $\gamma = 7$ is used to represent water (Batchelor, 1967), P_0 is the reference pressure. The pressure the equation of state solves for P, is then used in the SPH momentum equation governing the particle motion.

The time stepping in this code is explicit and is limited by the Courant condition modified for the presence of viscosity,

$$\Delta t = \min_a \left\{ 0.5h \middle/ \left(c_s + \frac{2\xi\mu_a}{h\rho_a} \right) \right\}, \tag{16}$$

where c_s is the local speed of sound.

3. Experimental procedure

The experimental set-up shown in Fig. 2 consists of a mechanical oscillator whose structure includes an inverted pendulum. Structural stiffness is provided by springs. It has been reported that the inverted pendulum arrangement can enhance the energy dissipation of a TLD up to 7-fold as compared to that experiencing pure translation (Lu et al., 2004).

A rectangular container to accommodate the sloshing liquid is mounted on the pendulum, 670 mm above the pivot point. Hence, as the structure is excited, the container is subjected to angular oscillations. Control is achieved with varying depths of water from 2.75 to 22 mm. Structural parameters and container dimensions are given in Table 1.

The disturbance is provided from an initial angular displacement of 16°. A simple stop-block allows consistent initial conditions for all cases. The structure is released from this initial position and allowed to oscillate freely. Experimental observations are video recorded with a standard digital camera, at a speed of 20 frames per second. Such frame speed is sufficient where the largest fundamental frequency of the structure is around 0.3 Hz.

The mass moment of inertia of the uncontrolled structure is measured to be approximately 3.2 kg m^2 about the centre of rotation. The ratio of mass moment of inertia of fluid (when the container is in the neutral horizontal position) to that of the structure for the above mentioned liquid depths are shown in Table 2, along with the corresponding mass ratios.

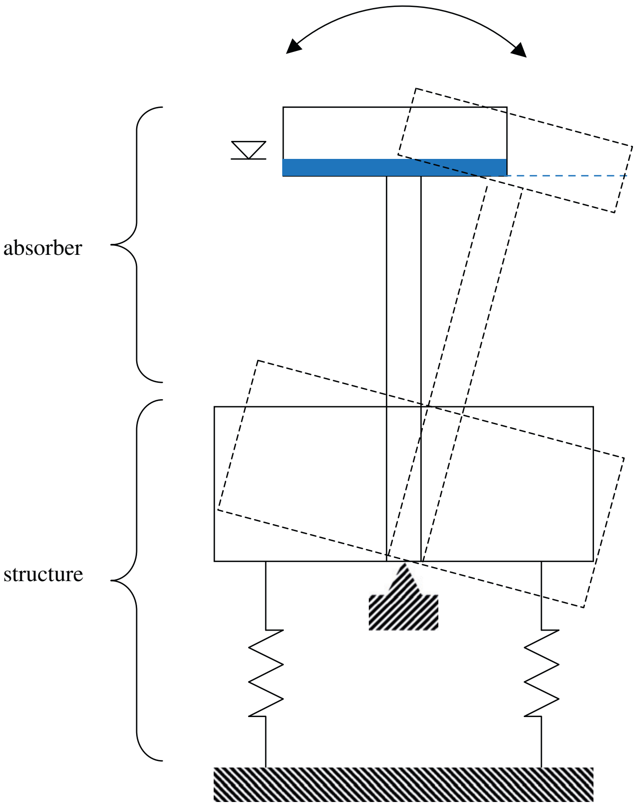

Fig. 2. Schematic showing the structure and the tuned absorber.

Table 1
Experimental parameters. Mass and length are reported with an estimated accuracy of 0.010 kg and 1 mm, respectively.

Mass (kg)	16.6
Equivalent viscous damping ratio	0.015 ± 0.002
Inertia-uncontrolled (kg m^2)	3.2
Container length × width × depth (mm^3)	340 × 230 × 142

Table 2
Ratios of rotary inertia and mass of fluid to those of the structure for different liquid depths.

Depth ± 0.25(mm)	Rotary inertia	Mass
2.75	1/32	1/80
5.5	1/16	1/40
8.25	1/10	1/26
11	1/8	1/20
22	1/4	1/10

4. Numerical procedure for kinematic predictions

The experimental set-up shown in Fig. 2 is modelled numerically using an SPH code developed by CSIRO's Mathematical and Information Sciences Division. As discussed earlier, SPH is a particle-based, rather than a conventional grid based method of modelling fluid flows.

A rigid container having the same experimental dimensions is placed 670 mm above the pivot point, replicating the structure arm seen in Fig. 2. It is then filled with different levels of water with a density of 1000 kg m^{-3} and viscosity of 0.001 Pa s. A particle cross-sectional area of 0.5 mm × 0.5 mm is used to produce enough resolution to capture all flow characteristics, without extending computational time unnecessarily. A resolution study has been completed, but is not shown here for brevity (Marsh, 2009). The time step used in all simulations is 2.5×10^{-5} s. The total simulation time is chosen to ensure all structure motion is modelled, from the point of release until motion has ceased, and therefore varies depending on liquid level.

Using 0.5 mm × 0.5 mm particles, 8404 SPH particles are needed to represent the system with 5.5 mm liquid depth, 6494 fluid particles, and 1910 boundary particles representing the container. At 22 mm liquid depth, 30 937 SPH particles are needed, 29 027 fluid particles, and 1910 boundary particles. A 3.2 GHz Xeon processor is used for computation.

To replicate the experimental conditions, the container is given an initial displacement of 16° clockwise, and allowed for 4 s to settle the fluid particles. Settling time is needed for the velocity of the fluid particles to drop down to 10^{-3} m/s at the container surface. All other fluid particles settle at lower velocity magnitudes. The experimentally observed motion of the container is then imposed on the numerical model to excite the fluid in two-dimensional space.

5. Numerical procedure for fluid–structure interaction predictions

For predictions of fluid–structure interaction, tethers are attached to the container, representing the force relationship between the structure and the absorber. This relationship exists due to the structure's stiffness and viscous damping properties. The container motion is restricted to dynamic rotation about its pivot point. The structure and sloshing absorber are subject to the same initial condition as before. Structural motion ceases due to the damping of the attached tethers, and the additional control of the working fluid.

6. Experimental observations

Angular displacement histories of the uncontrolled case, along with the 2.75, 5.5, 8.25, 11 and 22 mm liquid depth cases are shown in Figs. 3(a)–(f). The uncontrolled case in Fig. 3(a) experiences just over seven cycles of oscillation in the first 22 s. The frequency of oscillations decreases with the increasing amount of water in the absorber; 2.75 mm depth undergoes six full cycles of oscillation before coming to rest, whereas the 22 mm case experiences only one and a half cycles. The reduction of the frequency of oscillation is the result of negative stiffness imposed by the inverted pendulum configuration and (to a smaller extent) the added mass.

The behaviour observed at 2.75 and 5.5 mm depths is expected for an under-critically damped freely vibrating system (Rao, 1995). For the 8.25 mm depth, some interesting behaviour is observed during the third cycle of oscillation, around 10 s. At this instant, the pressure force exerted on the right container wall by the fluid is sufficient to change the structure's direction of motion. The 11 mm depth case exhibits similar behaviour to those of 2.75 and 5.5 mm depth. The response of the structure at 22 mm depth is drastically different, no longer possessing exponential decay to represent its behaviour; the excessive amount of added mass is assumed to be the reason for this.

The effectiveness of a sloshing absorber increases as free surface motion becomes more violent (Banerji et al., 2000). At shallow liquid depths of 2.75 and 5.5 mm, fluid motion is energetic. A strong hydraulic jump and wave breaking are observed. As liquid is added structural frequency becomes smaller, causing less violent free surface behaviour.

The equivalent damping ratio for each half-cycle in Fig. 3 is marked directly above displacement peaks. The magnitudes shown indicate the amount of damping produced by one full cycle of oscillation, ending at this peak, calculated from the logarithmic decrement of the structure's oscillations. Generally, damping increases as the number of cycles experienced by the structure increases. In all cases, besides 11 mm depth, the highest damping is observed in the last two cycles of oscillation. Damping also increases with liquid depth. The reason for this is presumed to be negative stiffness and added mass effects. All controlled cases produce a significant increase in damping relative to the uncontrolled case. This is due to both the control force the fluid exerts on the structure, and viscous dissipation within the sloshing fluid.

A summary of the settling times of all cases is shown in Fig. 4. The settling time is defined as the time taken from the instant of the structure's release to when its motion has ceased, residing in the central rest position. Cases employing any level of liquid produce considerable reductions in settling time, relative to that of the uncontrolled case. An optimum condition exists between the liquid depths of 2.75 and 8.25 mm, the marginally best performer being 5.5 mm.

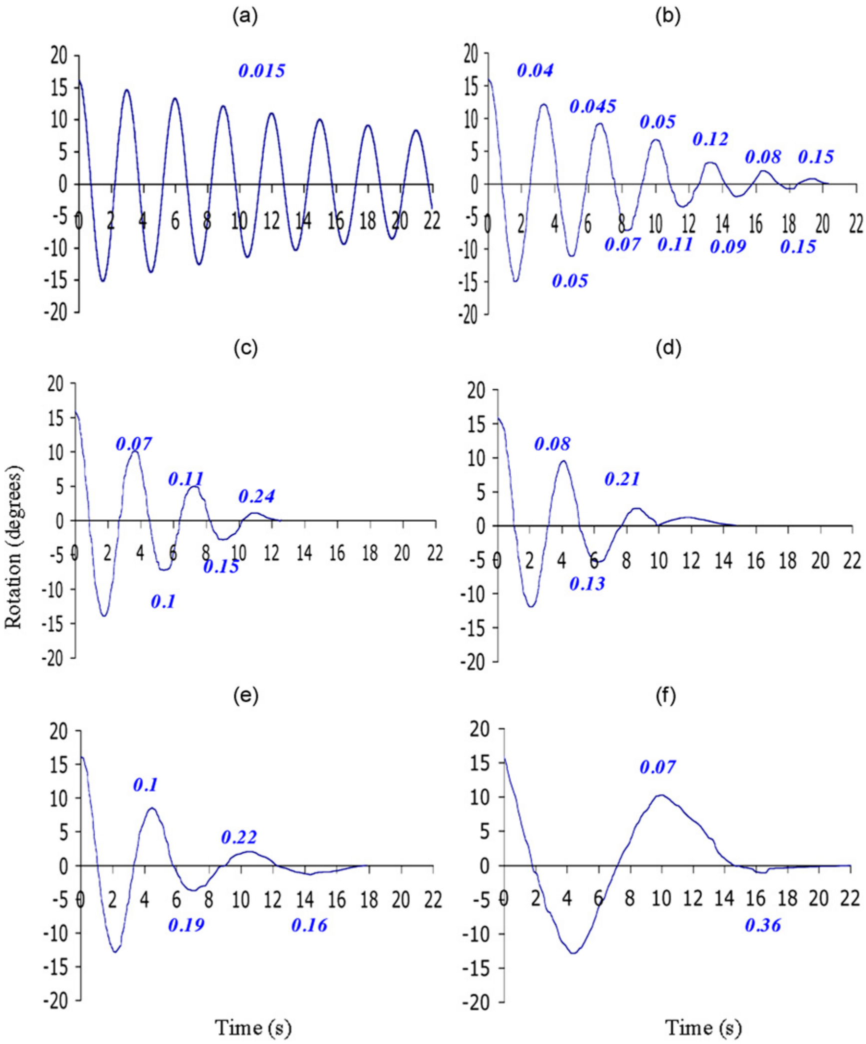

Fig. 3. Angular oscillation histories of: (a) uncontrolled, (b) 2.75 mm, (c) 5.5 mm, (d) 8.25 mm, (e) 11 mm, and (f) 22 mm deep cases.

Fig. 4. Variation of settling time with different water depths.

It is interesting to notice that the control performance of the sloshing absorber, at least in terms of settling time, is virtually independent of the liquid level for a significantly wide range to the right of 5.5 mm. Such an apparent insensitivity is a great advantage from a practical point of view.

These experimental observations clearly demonstrate the effectiveness of the suggested vibration controller in this section. Hence, further investigation into the physical events responsible for the dissipative qualities is certainly warranted. The widely used alternative, the optimally tuned dynamic vibration absorber, may still be the best controller requiring up to 20% critical damping ratios (Anderson et al., 2000). However, all damping devices are heavy maintenance items. The advantage of the sloshing absorber, on the other hand, is that it is virtually maintenance free. For this reason, a direct comparison of performance between the two control methods is not found necessary.

It is quite impractical to identify intricate flow behaviour through flow visualisation alone. Therefore, efforts have been made in numerical simulations which will be discussed in the following section. Once the accuracy of the modelling tool is established, efforts will be concentrated on design, focusing on enhancing the energy dissipation mechanism for better structural control.

7. Kinematic predictions

The nominated instances analysed in this section are chosen either as points of reference (when the structure is in the central rest position, or at peak displacement) or at points in time where fluid behaviour is interesting and/or difficult to capture numerically. The purpose of choosing these instances is to give a complete picture of the modelling tool's capabilities, as opposed to instances when only exceptional predictions are observed.

At the liquid depth of 2.75 mm, non-physical behaviour is predicted when modelling the fluid with a particle size of 0.5 mm × 0.5 mm. A higher resolution is required in shallow depths to accurately predict the behaviour at the free surface than that used in deeper liquid levels. Since the SPH model used does not have variable spatial resolution capabilities the resolution needed at the free surface must be used throughout the entire fluid volume. At the depth of 2.75 mm, the resolution required to accurately predict the behaviour at the free surface incurs a computational expense that is too high for the current computational capabilities. Hence, this depth is not presented here.

Free surface comparisons at 5.5 mm liquid depth are shown in Fig. 5. The left column represents experimental findings at certain instants in time, numerical predictions are shown in the right column. Figs. 5(a) and (b), (c) and (d), (e) and (f), (g) and (h), (i) and (j), (k) and (l), and (m) and (n), correspond to times of 0, 0.95, 1.30, 1.60, 1.85, 2.75 and 3.70 s, respectively, from the instant of release.

The structure supporting the sloshing absorber is set to an initial clockwise rotation of 16°. This instant is shown just prior to release in Fig. 5(a). The fluid is seen at the bottom right-hand corner of the container. The structure is held in this position until fluid motion is no longer noticeable. The numerical model in Fig. 5(b) emulates the same behaviour observed, after positioning the container and allowing the fluid particles to settle.

Once released, the structure rotates from right to left. Motion is energetic, passing through the central rest position at 0.95 s, as shown in Fig. 5(c). The structure's motion produces a travelling wave in the same direction. Fluid distribution and travelling wave development are predicted well in Fig. 5(d). However, the predicted free surface is somewhat bumpier than that observed.

At 1.30 s, in Figs. 5(e) and (f), the travelling wavefront collides with the left container wall. Fluid is distributed over the entire container bottom at this instant. Wave-to-wall interaction has only just commenced at the left side of the container. The numerical fluid distribution is comparable to that observed, but fluid has not yet fully reached the container wall.

Energetic wave-to-wall interaction ensues. Fluid flow is laminar and of high velocity (1.1–1.2 m/s at the wavefront) as it approaches the container wall. Sudden change in the direction of the container contact surface causes the fluid to climb the container wall, producing the strong moving surge hydraulic jump shown in Fig. 5(g). Such an event produces a rapid transition from a supercritical to subcritical regime fluid flow (Murzyn and Chanson, 2007; Sturm, 2001). Supercritical flow occurs when the fluid velocity (V_f) is larger than the shallow-water wave propagation speed C_0 (White, 2003), defined as

$$C_0 = \sqrt{h_f g}, \tag{17}$$

where h_f is the fluid depth and g is the acceleration due to gravity. Kinetic energy is transferred into potential energy due to the change in fluid elevation.

Hydraulic jump is predicted numerically, as shown in Fig. 5(h). The forecast fluid elevation of the hydraulic jump is similar to that observed experimentally. However, an exaggerated swirling flow pattern is predicted. The elevated fluid then collapses on itself under gravity. Flow becomes turbulent at this point in time, a characteristic of hydraulic jumps (Chanson, 1999). Steep velocity gradients are produced as a result, along with inherent viscous dissipation due to shear stress. A small amount of air entrainment is seen in the form of bubble formation in Fig. 5(h).

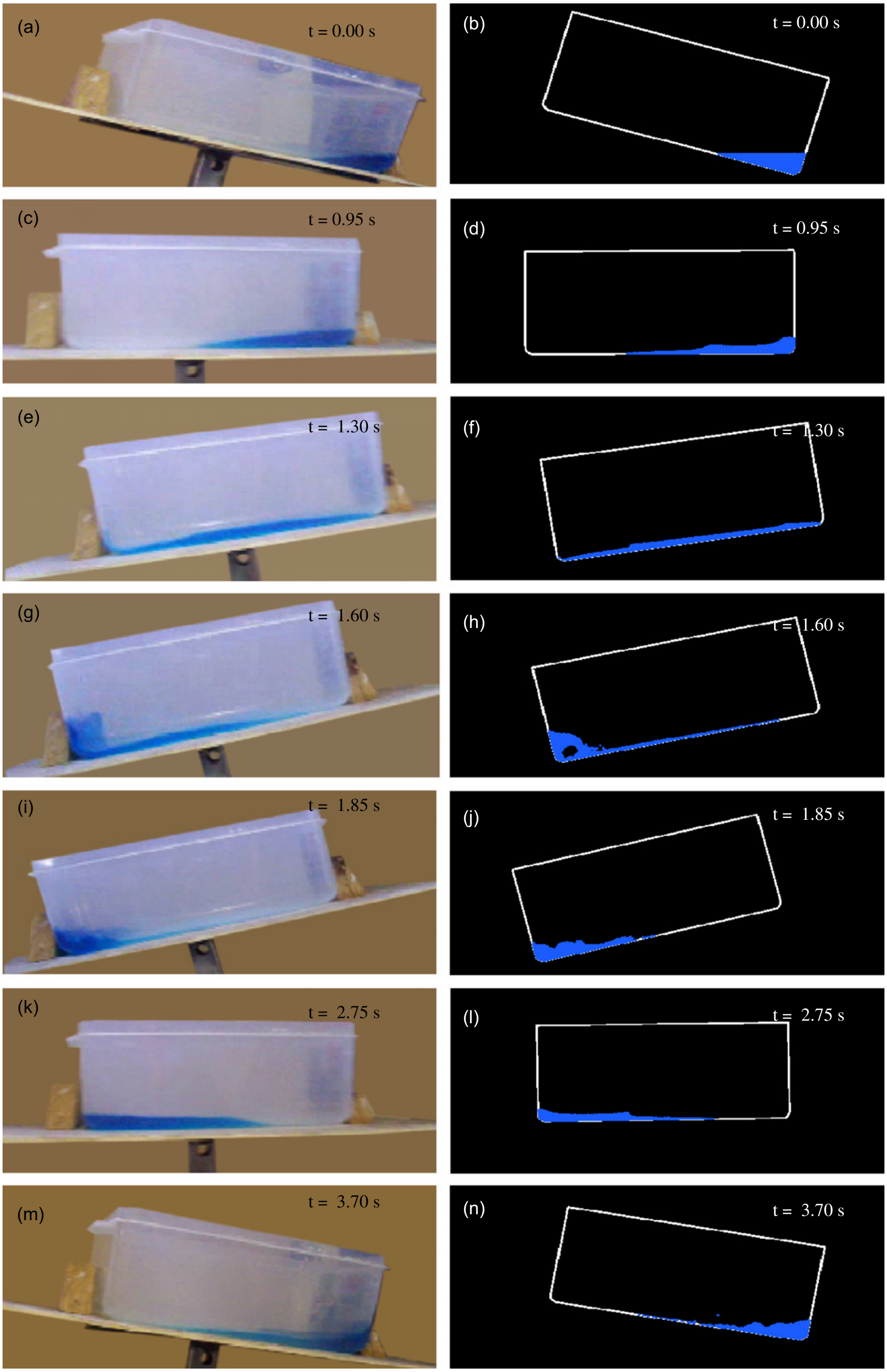

Fig. 5. Free surface comparisons of 5.5 mm liquid depth: left column has the experimental observations and right column has the numerical predictions.

The structure achieves maximum anti-clockwise rotation at 1.85 s. As shown in Fig. 5(i), the free surface is uneven due to swirling fluid behaviour at this time. Around 80% of the container length is exposed. The prediction in Fig. 5(j) exhibits a slightly sparser distribution; less than two-thirds of the container length is predicted to be dry. Swirling behaviour is also seen numerically.

The structural motion commences from left to right shortly after, producing a travelling wave in the same direction. In Fig. 5(k), the structure is passing through the central rest position at 2.75 s. The predicted fluid distribution agrees closely with that observed, as illustrated in Fig. 5(l). The free surface predicted is somewhat rougher than that observed experimentally.

Wave-to-wall interaction commences at 3.15 s, producing a smaller hydraulic jump of the same type, at the right container wall. Rotation in the clockwise direction ceases shortly after 3.70 s. The free surface shape at this instant, shown in Fig. 5(m), is smooth with around one-third of the container length is exposed. The predicted fluid behaviour differs from that observed, possessing the irregular free surface shape shown in Fig. 5(n). Almost two-thirds of the container length is predicted to be dry. Motion ceases at around 13 s.

From the comparison with the experimental results as presented in Fig. 5, the fluid distribution and position have been captured well numerically for 5.5 mm liquid depth. The travelling wavefront position is predicted accurately. Although this is the case, predicted free surface shapes are generally more uneven than those observed. This result is expected to be due to some bumpiness in the imposed motion. The main discrepancies in free surface shape and fluid behaviour are seen during wave-to-wall interactions. Exaggerated swirling behaviour is predicted during hydraulic jump, whilst the fluid is most energetic.

Free surface comparisons of the 22 mm liquid depth case are shown in Fig. 6. Figs. 6(a) and (b), (c) and (d), (e) and (f), (g) and (h), (i) and (j), (k) and (l), and (m) and (n), correspond to times of 0.00, 1.65, 2.00, 4.35, 6.00, 7.20 and 10.15 s, respectively, from the instant of the structure's release.

As in shallower depths, a travelling wave is produced in the direction of the structure's motion. Fig. 6(c) corresponds to 1.65 s after release. In contrast to lower liquid levels, the structure's motion is lethargic, the travelling wavefront having just collided with the left container wall. Undulating hydraulic jump is observed here, as opposed to the strong jump seen at lower liquid levels during the first wave-to-wall interaction. Minimal energy seems to be dissipated as a result, relative to shallower depths. The wavefront velocity is around 0.35 m/s. An undulating hydraulic jump is predicted accurately in Fig. 6(d).

Elevated, subcritical flow evolves into a travelling wave starting from the left wall, opposing the main body of fluid still moving in the opposite direction. This wave can be seen in Fig. 6(e) as the structure passes through the central rest position. The structure continues to rotate from right to left until maximum anti-clockwise rotation at 4.35 s, shown in Fig. 6(g). All kinetic energy has been converted to potential, the structure's motion has momentarily ceased, and all fluid mass resides in the left-hand side of the container. The corresponding simulation results are shown in Fig. 6(h) with an analogous fluid distribution.

As the structure oscillates back towards the central rest position, fluid flows from left to right almost touching the right container wall, as shown in Fig. 6(i), at 6 s. The numerical solution in Fig. 6(j) predicts a closely matching free surface shape. The free surface is smooth as the structure passes through the central rest position at $t = 7.20$ s, shown in Fig. 6(k). The numerical prediction in Fig. 6(l) is practically identical. The container comes to rest at a maximum clockwise rotation of around 10.5°, occurring at 10.15 s, shown in Fig. 6(m). Around one-third of the container bottom is dry. The numerical prediction shown in Fig. 6(n) is in agreement with the experimental observations. The motion ceases around 22.60 s.

All experimentally observed behaviour is replicated using SPH at the liquid depth of 22 mm. Differences between empirical and numerical free surface shapes are minimal, and the undulating hydraulic jump is predicted well. Free surface comparisons of 8.25 and 11 mm liquid depths have been completed but are not shown here since they provide little additional understanding. In these cases, fluid distribution is captured well numerically. Differences in the details of the free surface shape between experimental observations and predictions become less significant as liquid depth increases.

Based on this rather strict form of comparison, the numerical modelling tool is able to produce exceptional free surface predictions, the accuracy of which improves with increasing liquid depth. Hence, SPH has been found to be satisfactory for modelling liquid depths of 5.5 mm and higher, with imposed container motion, with the 0.5 mm × 0.5 mm resolution. Since these results are encouraging, SPH is used with full interaction to predict structural motion. The minor differences between experimental and numerical findings discussed here are not expected to be significant during fluid–structure interaction. This relative insensitivity to the details of the free surface is due to the fact that the control force exerted on the structure by the fluid is an integral effect of the liquid motion, rather than its minute details.

8. Preliminary fluid–structure interaction predictions

To further validate the model preliminary predictions of structural motion via full fluid–structure interaction are presented in this section. Two representative cases are shown, namely the uncontrolled structure (no fluid in the

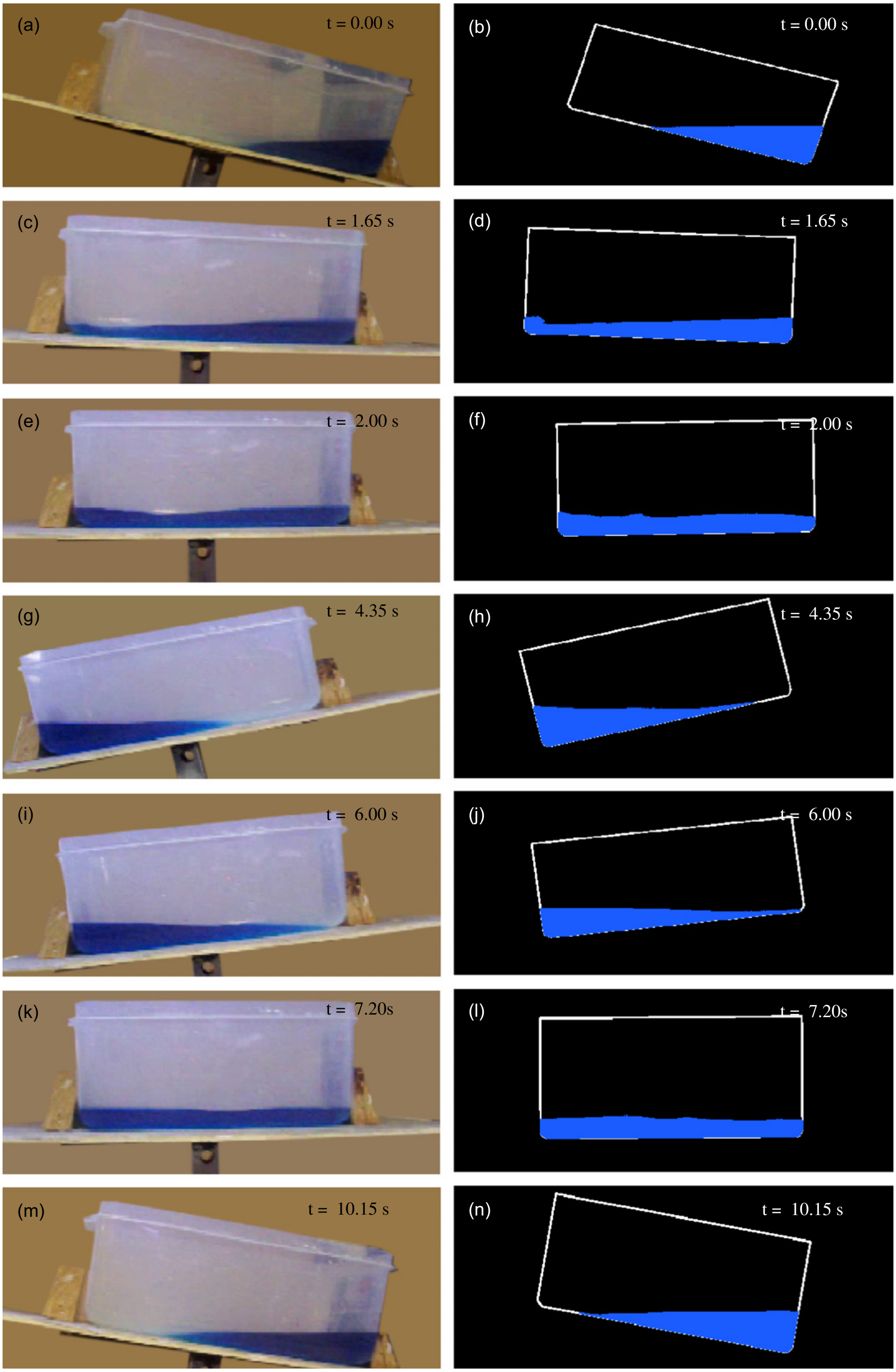

Fig. 6. Same as in Fig. 5, but for 22 mm liquid depth.

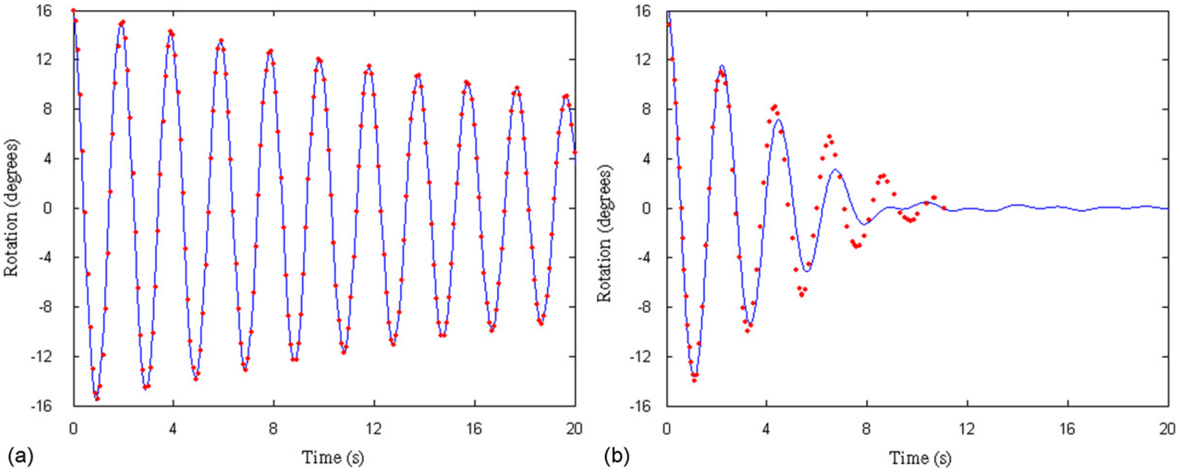

Fig. 7. History of angular displacement of the structure for experimental observations (●) and numerical predictions (—) of fluid–structure interaction for (a) the uncontrolled structure and (b) the structure controlled with 5.5 mm of liquid depth.

container), and with 5.5 mm of liquid depth. The latter is the shallowest liquid depth for which accurate free surface predictions are obtained for kinematic boundary motion.

The springs used to support the structure are replaced for fluid–structure interaction, increasing the structure's stiffness and natural frequency of oscillation. As a result, the fluid behaviour produced within the absorber is more energetic, and inherently difficult to capture numerically. Therefore, the preliminary evaluation of SPH to accurately predict the physics of fluid–structure interaction is critical, in a relative sense.

The observed angular displacement history of the structure is compared to the prediction obtained with SPH for the uncontrolled structure, along with the structure controlled by 5.5 mm of liquid depth, in Figs. 7(a) and (b), respectively. For the uncontrolled structure, SPH provides a precise prediction of its displacement. For the liquid depth of 5.5 mm, smaller peak structural displacements are predicted than observed. The emerging differences become more significant with increasing simulation time.

Although differences do exist between the predicted structure motion and that observed experimentally, they are marginal. Overall, structural behaviour and period of oscillation are predicted well, particularly during periods of high fluid kinetic energy. This demonstrates the potential of SPH to reliably model fluid–structure interactions between a structure and sloshing absorber. Hence, further investigation is certainly warranted.

9. Conclusions

Sloshing absorbers are promising vibration control agents for light resonant structures. They are of simple design, are cheap relative to the tuned mass damper (TMD) and other alternatives, and maintenance free due to the absence of mechanical parts such as springs and dashpots.

The primary form of energy dissipation in a sloshing liquid is shearing of the fluid, in the form of travelling and breaking waves and hydraulic jump. Shear stress is increased through providing steep velocity gradients. Wave-to-wall interactions are responsible for producing discontinuities in the flow field and, therefore, steep velocity gradients. A significant mechanism of energy dissipation in all depths is the hydraulic jump. Hence, this phenomenon should be encouraged. Energy dissipation caused by hydraulic jump is directly proportional to its height (Sturm, 2001). Jump height is maximised by producing a travelling wavefront of highest possible velocity, just prior to its collision with a container wall.

Generally, fluid distribution and free surface shape are predicted accurately. Details of wave-to-wall interaction at depths below 5.5 mm (where particularly strong hydraulic jumps are observed) differ slightly from those observed experimentally. Otherwise, fluid behaviour is predicted well.

The preliminary predictions of fluid–structure interaction identify the ability of the SPH method to accurately model the forces between a structure and sloshing absorber, when a liquid depth of 5.5 mm is employed. Hence, SPH is considered to be a useful tool for modelling the fluid behaviour within a sloshing absorber. However, the limitations of the method when predicting the dynamics of such systems are largely unknown. Efforts in identifying these limitations will be the next step of investigation.

Acknowledgements

This project is the end result of many fruitful suggestions from Professor Neil Popplewell of the University of Manitoba, Canada, who hosted a research sabbatical of the last two authors in 1999. Adam Marsh was a recipient of a Victoria University Postgraduate Scholarship and CSIRO Mathematical Information Sciences top-up Scholarship.

References

Anderson, J.G., Semercigil, S.E., Turan, Ö.F., 2000. A standing-wave type sloshing absorber to control transient oscillations. Journal of Sound and Vibration 232, 838–856.

Axisa, F., Antunes, J., 2007. Modelling of Mechanical Systems, vol. 3: Fluid–Structure interaction. Elsevier Butterworth-Heinemann, Oxford.

Banerji, P., Murudi, A., Shah, A.H., Poppelwell, N., 2000. Tuned liquid dampers for controlling earthquake response of structures. Journal of Earthquake Engineering and Structural Dynamics 29, 587–602.

Batchelor, G.K., 1967. An Introduction to Fluid Dynamics. Cambridge University Press, Cambridge.

Chanson, H., 1999. The Hydraulics of Open Channel Flow: An Introduction. Elsevier Butterworth-Heinemann, Oxford.

Cleary, P.W., 1998. Modelling confined multi-material heat and mass flows using SPH. Applied Mathematical Modelling 22, 981–993.

Cleary, P.W., Ha, J., Prakash, M., Nguyen, T., 2006. 3D SPH flow predictions and validation for high pressure die casting of automotive components. Applied Mathematical Modelling 30, 1406–1427.

Cleary, P.W., Prakash, M., Ha, J., Stokes, N., Scott, C., 2007. Smooth particle hydrodynamics: status and future potential. Progress in Computational Fluid Dynamics 7, 70–90.

Colagrossi, A., 2005. A meshless Lagrangian method for free surface and interface flows with fragmentation. Ph.D. Thesis, University of Rome La Sapienza, Italy.

Curadelli, O., Ambrosini, D., Mirasso, A., Amani, M., 2010. Resonant frequencies in an elevated spherical container partially filled with water: FEM and measurement. Journal of Fluids and Structures 26, 145–159.

Faltinsen, O.M., 1993. Sea Loads on Ships and Offshore Structures. Cambridge University Press, Cambridge.

Kareem, A., 1990. Reduction of wind induced motion utilising a tuned sloshing damper. Journal of Wind Engineering and Industrial Aerodynamics 36, 725–737.

Liu, G.R., Liu, M.B., 2003. Smoothed Particle Hydrodynamics, a Meshfree Particle Method. World Scientific Publishing, Singapore.

Lu, M.L., Poppelwell, N., Shah, A.H., Chan, J.K., 2004. Nutation damper undergoing a coupled motion. Journal of Vibration and Control 10, 1313–1334.

Marsh, A.P., 2009. Design of effective travelling-wave sloshing absorbers for structural control. Ph.D. Thesis, Victoria University, Australia.

Modi, V.J., Welt, F., Seto, M.L., 1996. Control of wind induced instabilities through application of nutation dampers: a brief overview. Journal of Engineering and Structures 17, 626–638.

Modi, V.J., Munshi, S.R., 1998. An efficient liquid sloshing damper for structural control. Journal of Fluids and Structures 12, 1055–1071.

Monaghan, J.J., 1992. Smoothed particle hydrodynamics. Annual Review of Astronomy and Astrophysics 30, 543–574.

Murzyn, F., Chanson, H., 2007. Free surface, bubbly flow and turbulence measurements in hydraulic jumps. Report CH63/07, Division of Civil Engineering, The University of Queensland, Brisbane, Australia (IBSN 9781864998917).

Païdoussis, M.P., 2008. Book review. Journal of Fluids and Structures 24, 446–448.

Popov, G., Sankar, S., Sankar, T.S., 1993. Dynamics of liquid sloshing in baffled and compartmented road containers. Journal of Fluids and Structures 7, 803–821.

Rao, S.S., 1995. Mechanical Vibrations, 3rd ed Addison-Wesley Publishing, Reading, MA.

Shekari, M.R., Khaji, N., Ahmadi, M.T., 2008. A coupled BE–FE study for evaluation of seismically isolated cylindrical liquid storage tanks considering fluid–structure interaction. Journal of Fluids and Structures 25, 567–585.

Sturm, T.W., 2001. Open Channel Hydraulics. McGraw-Hill, New York.

Sun, L.M., Fujino, Y., 1994. A semi-analytical model for tuned liquid damper (TLD) with wave breaking. Journal of Fluids and Structures 8, 471–488.

Tait, M.J., El Damatty, A.A., Isyumov, N., Siddique, M.R., 2005. Numerical flow models to simulate tuned liquid dampers (TLD) with slat screens. Journal of Fluids and Structures 20, 1007–1023.

Tamura, Y., Kohsaka, R., Nakamura, O., Miyashita, K., Modi, V.J., 1996. Wind-induced responses of an airport tower—efficiency of a tuned liquid damper. Journal of Wind Engineering 65, 121–131.

White, F., 2003. Fluid Mechanics. McGraw-Hill, New York.